

Matched-Filter Loss From Time-Varying Rough-Surface Reflection With a Small Effective Ensonified Area

Douglas A. Abraham, *Senior Member, IEEE*, Stefan M. Murphy, Paul C. Hines, and Anthony P. Lyons, *Member, IEEE*

Abstract—Active sonar sensing often entails propagation paths that include a surface reflection, particularly in shallow-water scenarios. Surface reflection loss, which degrades sonar performance, depends on how rough the surface is with respect to the sensing wavelength and grazing angle. The Rayleigh roughness measure quantifies this relationship with small values representing an acoustically smooth surface and large values an acoustically rough surface. Models predicting surface reflection loss are generally derived assuming the surface shape is not varying over the time in which the pulse is reflecting from it and that the ensonified region of the surface is large in extent relative to the spatial correlation length of the surface. While these models are often appropriate for short-duration narrowband pulses, they are not necessarily applicable to long-duration broadband pulses, which are the focus of this paper. By assuming the effective ensonified area after matched filtering is smaller in extent than the spatial correlation length, a surface-reflection-loss model is derived as a function of pulse duration relative to surface wave period when the net surface displacement is Gaussian distributed. As might be expected the matched filter loss for the small-ensonified-area scenario increases with the Rayleigh roughness, the number of consecutive surface reflections, and the ratio between pulse duration and the surface wave period. With respect to the latter, the loss is predicted to saturate when the pulse duration exceeds one surface wave period. The model was compared with data measurements from the 2013 Target and Reverberation Experiment, as reported by Hines *et al.* (“The dependence of signal coherence on sea surface roughness for high and low duty cycle sonars in a shallow water channel,” *IEEE J. Ocean. Eng.*, vol. 42, no. 2, pp. 298–318, Apr. 2017). The data represent both short- and long-duration pulses with respect to the surface wave period. For the short-duration pulses, the model corroborates the data analysis by Hines *et al.* in predicting a very small matched filter loss. It also compared very favorably with the data

for the long-duration pulses in both level and slope as a function of surface roughness. The models presented in this paper should be useful in sonar-equation analysis for predicting surface reflection loss with broadband waveforms when pulse duration is on par with or exceeds the surface wave period.

Index Terms—Coherence, matched filter, sonar, surface reflection loss, surface roughness, surface waves.

I. INTRODUCTION

REMOTE sensing with active sonar systems often involves indirect propagation paths reflecting from the ocean surface. When the surface is perfectly reflecting and smooth in shape with respect to the sensing wavelength the reflected pulse only undergoes a change in sign. However, when the surface is rough the reflected pulse is also attenuated, which will reduce sonar performance. A rough surface can arise from swell or wind-generated waves and models are readily available to describe the surface reflection loss as a function of wind speed (e.g., [1] or [2, Sec. 8.1.1]). These theoretical models for rough-surface reflection are generally derived under an assumption that the surface is static while the pulse reflects off of it (i.e., the “frozen” ocean assumption) and that an area large in extent relative to the spatial correlation length (SCL) of the surface is ensonified. A classic model [3] arising when the displacement from the smooth-surface condition (i.e., a flat surface) follows a Gaussian distribution results in a $4.3\gamma_r^2$ dB attenuation in the pressure for each reflection.¹ The quantity $\gamma_r = 2k_c\sigma_z \sin \theta_g$ is the Rayleigh roughness, where k_c is the acoustic wavenumber, σ_z is the root-mean-square (RMS) surface displacement, and θ_g is the grazing angle of the incident and reflected pulses as measured from the surface. The focus of this paper is on surface reflection loss when the *effective* ensonified area on the surface is small in dimension relative to the SCL and when the surface is in motion while the pulse reflects from it. Two design characteristics of an active sonar pulse motivate this focus: bandwidth and duration. The classic theory is generally adequate for short-duration narrowband (NB) pulses. However, broadband waveforms such as linear- and hyperbolic-frequency-modulated (LFM and HFM) pulses produce, after matched filtering, an effective ensonified area that is inversely proportional

Manuscript received September 17, 2016; revised February 13, 2017; accepted May 9, 2017. This work was supported by the Office of Naval Research Code 321 Undersea Signal Processing. This paper was presented in part at the 2016 MTS/IEEE OCEANS Conference, Monterey, CA, USA, Sep. 2016. (Corresponding author: Douglas A. Abraham.)

Associate Editor: A. Morozov.

D. A. Abraham is with CausaSci LLC, Ellicott City, MD 21041 USA (e-mail: abraham@ieee.org).

S. M. Murphy is with the Sonar and Anti-Submarine Warfare Group, Defence Research and Development Canada–Atlantic, Dartmouth, NS B2Y 3Z7 Canada (e-mail: stefan.murphy@drdc-rddc.gc.ca).

P. C. Hines is with the Department of Electrical and Computer Engineering, Dalhousie University, Halifax, NS B3H 4R2 Canada (e-mail: phines50@gmail.com).

A. P. Lyons is with the Center for Coastal and Ocean Mapping, University of New Hampshire, Durham, NH 03824 USA (e-mail: anthony.lyons@com.unh.edu).

Digital Object Identifier 10.1109/JOE.2017.2704198

¹Derivations of the classic surface reflection loss result can be found in [4, Sec. 13.2.1] or [5, App. A.3.3].

to bandwidth in the down-range dimension and can therefore be small relative to the SCL of the surface. When the surface is not so rough that the pulse compression properties of matched filtering are significantly impaired, the portion of the surface contributing to the match-filtered reflected wave, termed the *effective* ensonified area, depends (in the down-range dimension) on the bandwidth of the waveform rather than its duration as occurs for NB pulses. Noting that surface waves with periods of 4–12 s appear to dominate the wave energy spectrum [6, Ch. 9], the surface is expected to be effectively stationary for many sonar pulses. However, longer duration pulses are not uncommon in underwater acoustical applications (e.g., see [7]–[9]) and are therefore subject to a surface that is in motion throughout the reflection process.

This paper is organized in three sections. Modeling the surface reflection (see Section II), modeling sonar performance (see Section III), and a model-data comparison (see Section IV). The basic surface reflection geometry is described in Section II along with the classic surface-loss result for a Gaussian-distributed surface displacement. While broadband waveforms will clearly provide a small effective ensonified area in the down-range dimension, other factors are identified in Section II-C that can contribute to reducing the cross-range extent of the effective ensonified area. Given a small effective ensonified area, the reflected pulse is described as the incident pulse subject to a time-varying delay, which is related to the temporal variation in surface displacement. The ensuing distortion in the reflected pulse causes a mismatch loss in the matched filter (MF) that can be related to the surface displacement characteristics and sensing geometry. For a single surface reflection, the statistical characterization of the surface strongly influences the time-varying delay. When the surface comprises a large number of linearly combined waves, the Gaussian distribution is a natural candidate. As shown in Section II-F, it also arises in describing the net surface displacement encountered for a long-range sensing scenario within a waveguide, where there are multiple consecutive surface reflections. Research in the area of reflection and scattering from moving surfaces often focuses on the effect of Doppler (e.g., [10] and [11]), which is important in communications applications and is also affected by motion of the source and receiver. The loss of coherence [12]–[14], which can represent MF loss, has also been evaluated when the surface is in motion, although under the classical assumptions of a NB pulse and a large ensonified area. The small-effective-ensonified-area scenario with broadband waveforms appears only to have been considered in the data analysis and preliminary modeling reported by Hines *et al.* [9], which forms the motivation for the research presented in this paper as an expansion of [15]. By modeling the surface as a temporally bandpass space-time wide-sense-stationary (WSS) random process, the surface waves' dominant temporal frequency can be incorporated into the time-varying delay imparted to the pulse as it is reflected from a small effective ensonified area. As shown in Section III, this allows evaluation of the average loss incurred after matched filtering as a function of the pulse duration and bandwidth. While the modeling initially uses a NB analysis to provide tractable analytical results, both model and simulation results are presented for broadband LFM pulses.

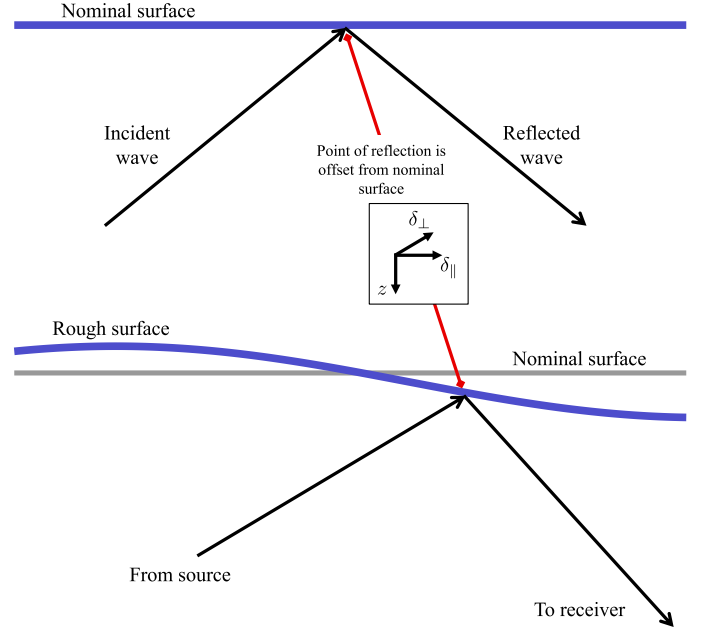


Fig. 1. Illustration of the displacement of the reflection point for a tilted surface relative to a smooth surface.

In Section IV, the models are compared to data measurements reported by Hines *et al.* [9] from the Office of Naval Research's 2013 Target and Reverberation Experiment (TREX-2013)² [16]. Two sensing scenarios from TREX13 are considered: A one-way/short-range/single-surface-reflection case (termed the “S1 path”) and a two-way/longer-range/multiple-surface-reflection case involving reflection from an air-hose (termed the “PATs echo”). While the details pertinent to the TREX13 data analysis are found in Section IV, the assumptions made developing the surface reflection loss models in Sections II and III will be related to the conditions encountered in the TREX13 data and environment when appropriate.

II. MODELING THE SURFACE REFLECTION

A. Surface-Reflection Geometry

Suppose a source and receiver are both at depth z_s and are separated by horizontal distance x_s . A pulse with analytic signal $p_0(t)$ is transmitted from the source, reflects from a smooth surface, and is measured at the receiver. Assuming the sound speed is constant, the point of specular reflection off the surface in the path connecting the source, surface, and receiver is halfway between the source and receiver. The reflection from this nominal surface is depicted in the upper part of Fig. 1, with a grazing angle θ_g relative to horizontal. The signal measured at the receiver

$$p_r(t) = a_r p_0(t - \tau_0) \quad (1)$$

is simply the transmitted signal subject to an amplitude scale (a_r) and a delay $\tau_0 = r_0/c_w$, where r_0 is the distance traveled and c_w is the speed of sound.

²See Section V for a full acknowledgement related to TREX13.

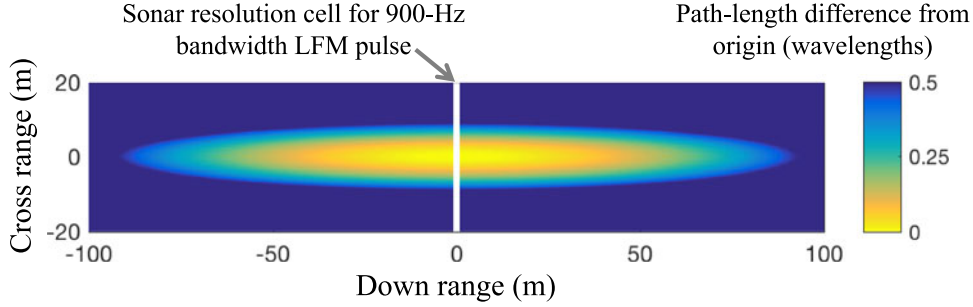


Fig. 2. Path-length difference for a single surface-reflection cycle of the PATS scenario in terms of wavelengths (clipped at 0.5) and the sonar resolution cell for a 900-Hz LFM pulse.

Now suppose the surface at the point of reflection is subject to small offsets in height and slope, as illustrated in the lower part of Fig. 1. This changes the surface-reflected path connecting the source and receiver, displacing the point of specular reflection from its original location on the nominal surface. Let $(\delta_{\parallel}, \delta_{\perp})$ represent the offsets in the horizontal plane with δ_{\parallel} in the parallel (\parallel) dimension (i.e., in the source-receiver plane) and δ_{\perp} as perpendicular (\perp) to that plane. Let z represent the vertical offset with $z > 0$ below the nominal surface. Note that z is used here rather than “ δ_z ” to emphasize that the reflection point is still a point on the surface. The difference in the path lengths between the perturbed and nominal surface geometries, when approximated by a MacLaurin series with first order in z and second order in δ_{\parallel} and δ_{\perp} , is

$$\Delta_r \approx -2z \sin(\theta_g) + \frac{\delta_{\parallel}^2}{z_s} \sin^3(\theta_g) + \frac{\delta_{\perp}^2}{z_s} \sin(\theta_g) \quad (2)$$

$$= -2z \sin(\theta_g) \left\{ 1 - \frac{\delta_{\parallel}^2 \sin^2(\theta_g)}{2zz_s} - \frac{\delta_{\perp}^2}{2zz_s} \right\} \quad (3)$$

$$\approx -2z \sin(\theta_g). \quad (4)$$

From (2) or (3), it can be seen that the second-order approximation requires the horizontal displacements (δ_{\parallel} and δ_{\perp}), which depend on the shape of the surface. The approximation in (4) retains only the first-order terms, assuming the conditions are met for the horizontal displacements to be small (e.g., a small RMS waveheight).

B. Classic Surface-Loss Result

Models of reflection from rough surfaces typically assume that the effective ensonified region of the surface is large relative to the SCL of the surface (n.b., a low-grazing-angle/far-field assumption may be required to produce an effective ensonified area encompassing many SCLs). For a pulse with duration D impinging on a surface at grazing angle θ_g , the ensonified down-range extent is $\mathcal{E}_{\parallel} = c_w D / \cos \theta_g$. As such, the large-ensonified-area assumption will generally be true for pulses with duration on the order of a second. The classic result (e.g., see [4, Sec. 13.2.1]) under this assumption uses (4) to obtain the loss in the average “coherent” pressure arising from reflection off a rough surface. In deriving the classic result, the surface height displacement is assumed to be static throughout the duration

of the pulse. The measured signal is then assumed to contain contributions from all possible surface displacements owing to the large ensonified area. This allows describing the measured signal as an expectation

$$p_r(t) = a_r E \left[p_0 \left(t - \tau_0 + \frac{2z \sin(\theta_g)}{c_w} \right) \right] \quad (5)$$

over all possible surface heights (z). As shown in [4, Sec. 13.2.1], when $p_0(t)$ is a sinusoidal signal with frequency f_c and the surface displacement z is modeled as Gaussian distributed with zero mean and variance σ_z^2 , the pressure measured at the receiver for a given time t has an amplitude lower than that for a fixed smooth surface by a factor $e^{-\gamma_r^2/2}$, where $\gamma_r = 2k_c \sigma_z \sin \theta_g$ is the Rayleigh parameter with wavenumber $k_c = 2\pi f_c / c_w$.

It is important to note that this reduction in the pressure amplitude does not accurately represent the loss incurred by a MF unless the coherent component dominates the total power (i.e., it will represent the MF loss only for small values of γ_r). Using the total power computation (e.g., see [17, Sec. 6.5]) produces the desired MF loss when the surface is stationary while the pulse reflects off it, but requires a statement about the SCL of the surface or the surface slope when γ_r is not small.

C. Small Effective Ensonified Area

The area of the surface ensonified by the sonar is (for low grazing angles) nominally defined in the down-range dimension by the pulse length and grazing angle and in the cross-range dimension by the transmitter beamwidth. However, the subset of the ensonified area contributing significantly to the specular reflection is limited to the first few Fresnel zones [18, Sec. 2.2]. To illustrate this, the path-length difference for one surface-reflection cycle of the PATS scenario is shown in Fig. 2, but limited to a maximum difference of one half wavelength to emphasize the first Fresnel zone.

The sonar and signal processing can also result in a reduction of the ensonified area contributing to the specular reflection. Of particular interest in this paper is the case of a broadband transmit waveform. Matched filtering broadband waveforms results in a sonar resolution cell with width approximately $1/W$, where W is the waveform bandwidth. This corresponds to the effective ensonified area having a down-range extent that is inversely proportional to bandwidth, $\mathcal{E}_{\parallel} = c_w / (W \cos \theta_g)$, rather than being

proportional to pulse duration as it is for NB pulses. For example, the very narrow sonar resolution cell for the 900-Hz LFM pulse used in the TREX13 experiment is shown in Fig. 2 for the PATS scenario. The 0.85-m down-range extent of the sonar resolution cell is significantly less than that of the first Fresnel zone. The effective ensonified area after Matched filtering can be viewed as the intersection between the sonar resolution cell and the first Fresnel zones. Thus, for the example shown in Fig. 2, pulse compression limits the effective ensonified area in the down-range dimension while the Fresnel zone limits it in the cross-range dimension. The “small” effective ensonified area assumption made in this paper further assumes the SCL is larger in each dimension than the intersection of the sonar resolution cell and Fresnel zone so the reflection is dominated by only one part of the surface.

In the cross-range dimension, there are multiple mechanisms by which the effective ensonified area can be limited.

- 1) Beamforming in either the transmitter or receiver reduces the cross-range extent of the effective ensonified area of the surface, although generally not as significantly as Matched filtering does to the down-range dimension. This may only be the limiting factor for very narrow beams or at short ranges.
- 2) As previously mentioned, the physics of reflection as quantified by the first few Fresnel zones can limit the effective ensonified area. For shallow grazing angles, the Fresnel zone is narrower in the cross-range dimension than in the down-range dimension (i.e., the phase changes more rapidly in the cross-range dimension than down-range). This can be seen from (2), where the change in the path length with respect to the squared horizontal offset (δ_{\parallel}^2 or δ_{\perp}^2) is proportional to $\sin^3(\theta_g)$ in the down-range dimension whereas it is only proportional to $\sin \theta_g$ in cross-range, so an offset in the down-range dimension must be a factor $1/\sin \theta_g$ larger than a cross-range offset to yield an equivalent change in path length.
- 3) The SCL measurements, which can be formed from the ratio of the RMS wave height to the RMS surface slope as done in [9], primarily focus on the mainlobe of the spatial correlation function (SCF). They do not capture regions of high correlation induced by spatial periodicity of surface waves. These regions of high correlation outside the mainlobe of the SCF act to reduce the net surface variability (i.e., the number of statistically independent surface heights observed) within the effective ensonified area.
- 4) In a shallow-water sensing scenario where there are multiple surface-reflection cycles, reflection in the specular direction of the smooth surface (i.e., from horizontal facets) may dominate as other directions will fail to propagate down the waveguide [2, Sec. 8.1.1]. Thus, the small-effective-ensonified-area definition changes to require observing only one horizontal facet. This suggests using either one half of a spatial wavelength (if the surface is spatially periodic) or perhaps the distance to the first negative sidelobe in the SCF to define the SCL.

Of these mechanisms, only beamforming is under the control of a sonar designer. The others are either a byproduct of the sensing geometry or depend on the shape of the surface SCF.

When the effective ensonified area of the surface is small in extent relative to the SCL and the surface is smooth with a radius of curvature that is large relative to the acoustic wavelength, the tangent-plane scattering assumption inherent in the geometric representation of Section II-A is all that is necessary to describe reflection of the pulse.³ Because only a small, very correlated portion of the surface is effectively contributing to the reflection, the signal measured at the receiver can be represented by (1) with a time-varying delay defined by the height of the one contributing part of the surface. In the case where the pulse is short relative to the wave period, the wave can be assumed stationary throughout the reflection (i.e., the frozen ocean assumption). This implies the one part of the surface contributing to the reflection does not change during pulse reflection, it is at a constant height. The signal measured at the receiver is then of the form found in (1) with a delay $\tau_0 - 2z \sin(\theta_g)/c_w$. This is the opposite extreme of the large ensonified area assumed in the classic surface-loss result; here there is no combination over multiple surface heights but rather only one fixed surface height contributing to the reflection and resulting in no more than a small change in travel time. This implies that broadband pulses that are short in duration relative to the wave period will suffer little to no loss during surface reflection if the effective ensonified area is less than the SCL.

D. Time-Varying Delay

If the pulse duration is on the order of, or larger than, the wave period, the time-delay imparted on the reflected pulse can no longer be assumed constant; it must change with the surface displacement. Under the small-effective-ensonified-area conditions of Section II-C, (1) becomes

$$p_r(t) = a_r p_0(t - \tau_0(t)). \quad (6)$$

When (4) is a good approximation to the effect of displacing the point of specular reflection, the time-varying delay is dominated by the vertical displacement of the surface itself. Mathematically, if $Z(t, \vec{x})$ is the surface displacement as a function of time and space in the horizontal plane with $\vec{x} = (x_{\parallel}, x_{\perp})$, the time-varying vertical displacement of the reflection point is

$$z(t) = Z(t, \vec{x}_0 + \vec{\delta}(t)) \quad (7)$$

where $\vec{\delta}(t) = (\delta_{\parallel}(t), \delta_{\perp}(t))$ is the horizontal displacement from the reflection point of the nominal surface, which is assumed to be at \vec{x}_0 . As long as the horizontal displacement is small, $z(t)$ will be very similar in its statistical characteristics to the surface height at \vec{x}_0 ; that is, from a statistical perspective $z(t) \approx Z(t, \vec{x}_0)$.

Using the approximation in (4) with a time-varying vertical displacement in (6) produces

$$p_r(t) = a_r p_0(t - \tau_0 + 2c_w^{-1} z(t) \sin \theta_g) \quad (8)$$

³Ignoring the effects of shadowing and multiple scattering.

at the receiver where it is assumed that there is no change in the amplitude from either the longer propagation path or the small change in grazing angle associated with a displaced reflection point. As an example, suppose the vertical surface displacement has constant speed, $z(t) = v_s t$, then (8) results in $p_r(t) = p_0(\zeta t - \tau_0)$ where

$$\zeta = 1 + \frac{2v_s \sin \theta_g}{c_w} \quad (9)$$

is the familiar Doppler-induced time scale. However, as will be described in the following section, a more realistic model of the surface motion is desired before evaluating the impact on sonar performance.

E. Time-Varying Surface

Wind-generated surface waves, while not pure sinusoids, often have narrow spectral content. For example, both the Pierson–Moskowitz and Joint North Sea Wave Observation Project (JONSWAP) spectra [19, Sec. 16.4] exhibit increasingly narrow spectra as wind speed increases. A natural model for the surface displacement is therefore one of a temporally NB space-time random process

$$Z(t, \vec{x}) = A(t, \vec{x}) \cos(2\pi f_w t + \phi(t, \vec{x})) \quad (10)$$

where f_w is the dominant wave frequency in cycles per second (hertz). $A(t, \vec{x})$ and $\phi(t, \vec{x})$ represent temporally and spatially varying amplitude and phase and are assumed to be constructed so that $Z(t, \vec{x})$ is a zero-mean, WSS random process. The temporal variation of $A(t, \vec{x})$ and $\phi(t, \vec{x})$ should be slow relative to the frequency f_w for the surface height to be considered NB; however, the bandwidth only needs to be less than $2f_w$ (when centered at f_w) for (10) to represent a band-limited process. As an example, suppose $\phi(t, \vec{x}) = \vec{k}_w \cdot \vec{x} + \phi_0$ where ϕ_0 is uniformly random on $(0, 2\pi)$ and $A(t, \vec{x})$ is constant. The surface is then purely sinusoidal with the wave frequency f_w and wavenumber vector \vec{k}_w related by the appropriate wave dispersion equation. A band-pass nature implies that the mean-square surface displacement

$$\sigma_z^2 = E[Z^2(t, \vec{x})] = \frac{1}{2} E[A^2(t, \vec{x})] \quad (11)$$

is half the average power in the wave amplitude $A(t, \vec{x})$. For the purely sinusoidal surface with amplitude A_w , this results in $\sigma_z^2 = A_w^2/2$.

F. Multiple Consecutive Surface Reflections

In the remote-sensing scenario of interest, the propagating pulse is assumed to reflect off the surface n_s times consecutively as it travels down a waveguide. Suppose the surface reflections occur at locations \vec{x}_i and times $t + \tau_i$ for $i = 1, \dots, n_s$. Assuming the model of (4) where the time delay induced by the moving surface is dominated by the surface's vertical displacement at the point of reflection, the effect on the measured signal at a

receiver is that of a net displacement

$$\begin{aligned} z(t) &\approx \sum_{i=1}^{n_s} Z(t + \tau_i, \vec{x}_i) \\ &= \sum_{i=1}^{n_s} A(t + \tau_i, \vec{x}_i) \cos(2\pi f_w(t + \tau_i) + \phi(t + \tau_i, \vec{x}_i)) \\ &= \sum_{i=1}^{n_s} A_i \cos(2\pi f_w t + \phi_i) \end{aligned} \quad (12)$$

where A_i and ϕ_i represent the amplitude and net phase offset, respectively, from each reflection.

When the surface displacement is not purely sinusoidal, it is reasonable to assume it is statistically independent when sampled far enough apart in time and/or space. Such an assumption in the TREX13 environment is supported by the decaying SCFs found in [9]. Under the statistical independence assumption, the central limit theorem (CLT) [20, Sec. 5.3.2] can be applied to simplify the characterization of $z(t)$. First note that $\cos(2\pi f_w t + \phi_i) = \text{Real}\{e^{j2\pi f_w t + j\phi_i}\}$. Then

$$z(t) = \text{Real}\left\{e^{j2\pi f_w t} \sum_{i=1}^{n_s} A_i e^{j\phi_i}\right\} \quad (13)$$

$$= \sqrt{2\sigma_z^2 n_s} \text{Real}\{e^{j2\pi f_w t} V\} \quad (14)$$

where $E[A_i^2] = 2\sigma_z^2$ from (11) and, under some mild regularity restrictions on the distribution of (10)

$$V = \frac{1}{\sqrt{2\sigma_z^2 n_s}} \sum_{i=1}^{n_s} A_i e^{j\phi_i} \quad (15)$$

is approximately a zero-mean, unit-variance, complex Gaussian random variable. V can then be described in polar form as $V = A e^{j\phi}$, where A is Rayleigh distributed with unit power (i.e., $E[A^2] = 1$) and ϕ is uniformly random on $(0, 2\pi)$. This simplifies $z(t)$ to

$$z(t) = \sqrt{2\sigma_z^2 n_s} A \cos(2\pi f_w t + \phi) \quad (16)$$

and implies that for a given time, the net displacement is a zero-mean Gaussian-distributed random variable with variance $n_s \sigma_z^2$. Owing to the CLT applied to the sum in (13), this result is valid even when the surface displacement at a single point is not Gaussian distributed. The accuracy, of course, depends on how many surface reflections occur, unless $Z(t, \vec{x})$ is initially a Gaussian random process in which case the result is accurate for all n_s , even a single reflection.

III. SONAR PERFORMANCE MODELING

A. MF Loss and the Static-Surface Result

Sonar detection processing involves applying an MF to the received signal in (8), which represents the small-effective-ensonified-area scenario, using the transmit waveform as a replica

$$x(\tau) = \int_{-\infty}^{\infty} p_0(t) p_r^*(t + \tau) dt. \quad (17)$$

Because $p_0(t)$ and $p_r(t)$ are formulated as analytic signals, $x(\tau)$ is the complex envelope of the MF output. Detection is therefore accomplished by comparing the instantaneous intensity $|x(\tau)|^2$ to a threshold for all delays τ .

When the surface displacement is static (i.e., $z(t) = z_0$) the MF complex envelope is a scaled and delayed version of the waveform autocorrelation function (ACF)

$$x(\tau) = a_r \chi(\tau - \tau_1) \quad (18)$$

where $\chi(\tau) = \int_{-\infty}^{\infty} p_0(t) p_0^*(t + \tau) dt$ is the ACF of the transmit waveform. The delay $\tau = \tau_1 = \tau_0 - 2c_w^{-1} z_0 \sin \theta_g$ is where (18) will have a maximum squared envelope, $|a_r \chi(0)|^2$.

The loss in sonar performance arising from rough-surface reflection can be described by the reduction in the average peak signal intensity after Matched filtering, quantified by the loss factor

$$\bar{L} = \frac{1}{|a_r \chi(0)|^2} E \left[\max_{\tau} |x(\tau)|^2 \right] \quad (19)$$

where $|a_r \chi(0)|^2$ represents the smooth-surface result.

While the delay time τ_1 at which the peak MF output in (18) occurs will vary with z_0 , there is no loss (i.e., $\bar{L} = 1$) when the surface is static throughout the duration of a pulse and the effective ensonified area is small relative to the surface SCL. The scenario in which a loss might occur with a static surface displacement is when multiple different time delays are included in the measured signal for every realization of the surface (i.e., the scenario of the classic result described in Section II-B). However, the focus of this paper is on how much loss is incurred when the surface is in motion while the pulse is reflecting off it.

B. NB Modeling Results for a Time-Varying Surface

When the surface is in motion throughout the duration of the pulse, the time-varying surface height in (16) can be used to determine the MF loss for a given pulse type. While our primary interest lies in broadband waveforms because they yield a small effective ensonified area after Matched filtering, it is useful to consider the analytical results under the NB assumption of a small bandwidth relative to center frequency, which is essentially the same (in a mathematical sense) as assuming a continuous-wave (CW) pulse. Noting that the ACF width for a CW pulse is proportional to its duration, notionally there is a potential conflict between the need for a *short* CW pulse to induce a small ensonified area and at the same time a *long* pulse to observe changing surface motion (i.e., there may not be many CW-pulse-duration/surface-period/SCL conditions satisfying this scenario). Despite this limitation, the analytical results for the NB model are expected to be accurate for broadband pulses when the bandwidth-to-center frequency ratio (W/f_c) is small and they provide a mathematically tractable solution. This is conceptually similar to assuming the Doppler effect produces a frequency shift rather than a scale; it will be accurate if the waveform bandwidth is small enough relative to its center frequency.

The MF output of the received signal can be obtained by using (16) in (8) and then (17) to produce

$$x(\tau) = a_r^* \int_{-\infty}^{\infty} p_0(t) \times p_0^* \left(t + \tau - \tau_0 + \frac{2 \sin(\theta_g)}{c_w} \sqrt{2\sigma_z^2 n_s} A \cos(\omega_w t + \phi) \right) dt \quad (20)$$

where $\omega_w = 2\pi f_w$. To simplify the analysis, the peak magnitude of (20) is assumed to occur for the delay time matching that of the smooth surface ($\tau = \tau_0$). This essentially assumes any potential offset of the peak in delay from τ_0 arising from a distortion of the MF response is less than the temporal resolution of the waveform. Note that the offset of the peak here arises from an overly distorted MF response; it is not referring to a displacement of the effective ensonified area of the surface from the smooth-surface specular point as may occur in some surface/sensing-geometry scenarios (in which case τ_0 would be the travel time from the source to the displaced reflection point and then to the receiver). For CW pulses, the temporal resolution is proportional to duration and so this approximation is expected to be valid. However, for broad-band waveforms this may not be true. An additional approximation in the following analysis is that the integral in (20) will be restricted to $t \in (0, D)$, where D is the pulse duration. This approximation ignores the situations where the argument of p_0^* in (20) is outside of $(0, D)$ when $t \in (0, D)$ and $\tau = \tau_0$. When D is large relative to the maximum change in the integral limits, $2c_w^{-1} \sin(\theta_g) \sqrt{2\sigma_z^2 n_s}$, the approximation will be valid. Recall that active sonar processing for LFM and HFM waveforms uses a single MF to detect targets over a wide range of radial velocities [21, Sec. 5.3.3] because of their insensitivity to Doppler. The MF response in (20) is therefore formed assuming there is no Doppler effect in the replica waveform. Analysis of the impact of Doppler on sonar pulses most commonly assumes a constant relative radial velocity throughout the reflection process and results in the waveform ambiguity function (e.g., see [22, Sec. 5.1] for NB waveforms or [23] for broadband waveforms). While this could be used to obtain the MF response when the pulse is short relative to the wave period, it is not applicable when there is variation in the Doppler scale throughout the duration of the pulse as described by (20). However, as noted in Section II-D, the Doppler effect imparted by the moving surface is embodied in the time-varying delay found in the reflected signal in (20).

For a CW pulse with duration D and amplitude a_0 at radian frequency $\omega_c = 2\pi f_c$, the analytic signal is simply $p_0(t) = a_0 e^{j\omega_c t}$ for $t \in (0, D)$ and zero elsewhere. Inserting this into (20), subject to the aforementioned approximations, results in

$$x(\tau_0) \approx a_r^* |a_0|^2 \int_0^D e^{-j\sqrt{2\beta} A \cos(\omega_w t + \phi)} dt \quad (21)$$

where $\beta = n_s \gamma_r^2$. Assuming the delay τ_0 achieves the maximum MF response, the MF loss for a given realization of the surface displacement $Z(t, \vec{x})$, which is quantified by the random

variables A and ϕ , is

$$L(A, \phi) = \frac{|x(\tau_0)|^2}{|a_r \chi(0)|^2}. \quad (22)$$

The average MF loss is then an expectation over A and ϕ

$$\bar{L} = E[L(A, \phi)] \quad (23)$$

$$= E \left[D^{-2} \iint_0^D \exp \left\{ j \sqrt{2\beta} A [\cos(\omega_w t + \phi) - \cos(\omega_w s + \phi)] \right\} dt ds \right] \quad (24)$$

where $\chi(0) = D|a_0|^2$ for a pulse with duration D and a constant envelope a_0 . To simplify (24), note that the difference of cosines can be described as a product

$$\cos(\omega_w t + \phi) - \cos(\omega_w s + \phi) = m(t-s) \cos(\phi + \theta(t, s)) \quad (25)$$

where

$$m^2(t-s) = 2[1 - \cos(\omega_w(t-s))] \quad (26)$$

and the particular form of $\theta(t, s)$ is not necessary in the following analysis except to note that it does not depend on ϕ . Taking the expectation over ϕ inside the integrals over t and s results in a requirement for the integral

$$\frac{1}{2\pi} \int_0^{2\pi} \exp\{j\kappa \cos \phi\} d\phi = J_0(\kappa) \quad (27)$$

where the solution from [24, eqs. 3.715-13 and 3.715-18] is $J_0(\kappa)$, the zeroth order Bessel function. Using (27) in (24), taking the expectation over A inside the integrals and changing variables to $y = a^2$ results in

$$\bar{L} = D^{-2} \iint_0^D \int_0^\infty J_0(\sqrt{2\beta}m(t-s)\sqrt{y}) e^{-y} dy dt ds \quad (28)$$

$$= D^{-2} \iint_0^D \exp\{-\beta m^2(t-s)/2\} dt ds \quad (29)$$

$$= 2D^{-2} \int_0^D (D-u) \exp\{-\beta m^2(u)/2\} du \quad (30)$$

where the solution to the integral over y in (28) is from [24, eq. 6.614-1] and the dependence of the integrand in (29) on $u = t - s$ is exploited to simplify the double integral into a single integral. Substituting (26) into (30) results in the average MF loss

$$\bar{L}(Df_w, \beta) = \frac{e^{-\beta}}{\pi Df_w} \int_0^{2\pi Df_w} \left(1 - \frac{v}{2\pi Df_w}\right) e^{\beta \cos(v)} dv. \quad (31)$$

Note that \bar{L} depends on the product Df_w , which is the pulse duration in terms of surface-wave periods, and the net squared roughness, $\beta = n_s \gamma_r^2$. We will generally evaluate the models as a function of the quantity $\sqrt{\beta} = \sqrt{n_s} \gamma_r$, which will be called the net Rayleigh roughness (NRR).

When the pulse duration is much larger than the surface period ($Df_w \gg 1$) the integral $I_0(z) = (1/\pi) \int_0^\pi e^{z \cos x} dx$ from [24,

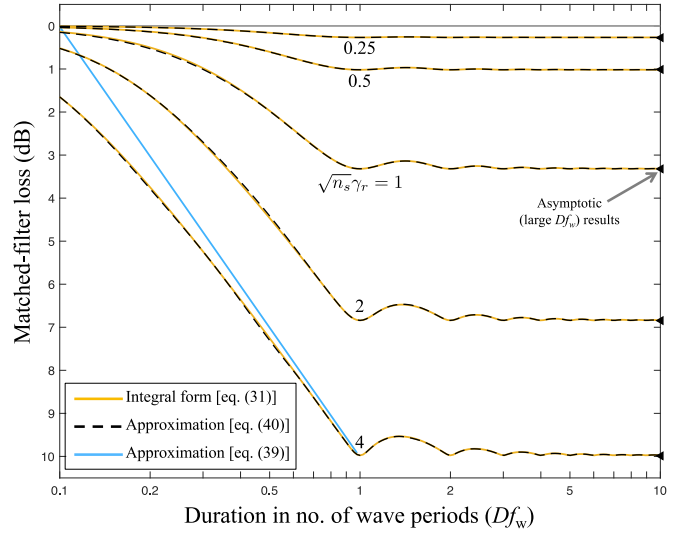


Fig. 3. MF loss as a function of pulse duration in terms of surface wave periods (Df_w) for various values of NRR ($\sqrt{n_s} \gamma_r$). The approximation from (39) is only shown for $\sqrt{n_s} \gamma_r = 4$.

eq. 3.339], which describes the zeroth-order modified Bessel function, can be used to obtain an asymptotic (in terms of large Df_w) value of the MF loss

$$\bar{L}_\infty = \bar{L}(\infty, \beta) = e^{-\beta} I_0(\beta) \quad (32)$$

only depending on the net squared roughness.

Numerical evaluation of (31) is shown in Fig. 3 (the gold colored lines under the black dashed lines) as a function of Df_w for various values of NRR ranging from 0.25 to 4. Note that the loss is shown in decibels as $-10 \log_{10} \bar{L}$. For a given NRR, the loss increases from 0 dB when the pulse is very short until $Df_w = 1$, above which it exhibits minor oscillations as it converges to \bar{L}_∞ . This implies that the asymptotic value may be an adequate approximation as long as $Df_w \geq 1$. The asymptotic MF loss (\bar{L}_∞) is shown in Fig. 4 as a function of the Rayleigh roughness (note this is γ_r , not NRR) for different numbers of surface reflections. As one would expect, the MF loss increases as either the Rayleigh roughness or number of surface reflections increases.

1) *Approximations to the Asymptotic Average Loss for the NB Model:* In sonar-equation analysis, the effect of reflection from a rough surface is commonly described as a “per-bounce” loss in SNR or increase in propagation loss. When using the coherent-pressure result for a large ensonified area as described in Section II-B, this results in a loss of $10\gamma_r^2 / \ln(10) \approx 4.3\gamma_r^2$ dB per reflection (e.g., see [25]).

The per-reflection loss for the small-effective-ensonified-area result can be derived by differentiating the loss in decibels with respect to n_s . Applying this process to the $Df_w \gg 1$ case represented by (32) results in

$$\frac{\partial}{\partial n_s} \{-10 \log_{10} \bar{L}_\infty\} = 4.3\gamma_r^2 \left[1 - \frac{I_1(n_s \gamma_r^2)}{I_0(n_s \gamma_r^2)} \right] \quad (33)$$

where β has been written as $n_s \gamma_r^2$ to emphasize the dependence of (33) on n_s and $I_1(\cdot)$ is the first-order modified Bessel func-

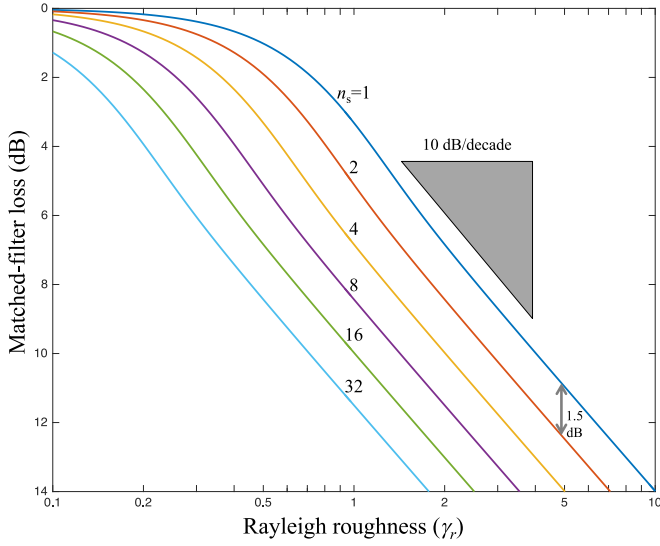


Fig. 4. Asymptotic (i.e., large Df_w) MF loss as a function of the Rayleigh roughness (γ_r) for various number of surface reflections.

tion. Using a small-argument expansion of the Bessel function from [26, Ch. 49] leads to

$$\frac{\partial}{\partial n_s} \{-10 \log_{10} \bar{L}_\infty\} \approx 4.3 \gamma_r^2 \left[1 - \frac{n_s \gamma_r^2}{2 + n_s^2 \gamma_r^4 / 4} \right] \quad (34)$$

for the MF loss when $n_s \gamma_r^2 \ll 1$. This indicates that, subject to low NRR, the result is similar for both the large-ensonified-area/short-pulse and the small-effective-ensonified-area/long-pulse scenarios. As described in [9], the proximity of these two results may be explained by noting that when $Df_w \gg 1$, the pulse interacts with many cycles of the surface. When roughness is very low (e.g., dominated by the coherently reflected pressure), this is in some manner similar to the averaging over all possible surface heights enacted in the coherent-pressure loss result.

However, the dependence on n_s observed in (33) indicates that increasing the number of reflections results in a decreasing rather than a constant loss per reflection. This likely arises from a partial cancellation of delays and advances encountered in separate reflections. To examine this, an expansion of $I_0(x)$ for large arguments from [26, Ch. 49] is used to approximate (32), resulting in

$$\begin{aligned} -10 \log_{10} \bar{L}_\infty \approx & 4 + 10 \log_{10} \gamma_r + 5 \log_{10} n_s \\ & - 10 \log_{10} \left\{ 1 + \frac{1}{8 n_s \gamma_r^2} \right\} \text{ dB.} \end{aligned} \quad (35)$$

The approximation is accurate to within 0.2 dB when $n_s \gamma_r^2 \geq 1$ and indicates that, for pulse durations such that $Df_w \geq 1$, propagation loss in decibels increases (approximately) according to $10 \log_{10} \gamma_r$ and $5 \log_{10} n_s$ when $n_s \gamma_r^2 > 1$. Both of these effects are evident in Fig. 4, with the latter producing the 1.5-dB separation between each doubling of n_s seen for $\gamma_r > 1/\sqrt{n_s}$. Thus, when NRR becomes large enough, additional surface reflections have less impact on sonar performance than for low-NRR scenarios. In particular, the approximately linear accumulation

of loss in decibels with γ_r^2 represented by (34) is only valid while $n_s \gamma_r^2$ remains small. This is likely similar to the large-ensonified-area result when MF loss is characterized by the total power.

2) *Approximations to the Average Loss for the NB Model:* As previously described, when the pulse duration is much shorter than the wave period ($Df_w \ll 1$), there is negligible loss in the MF. To illustrate this and to examine how the per-reflection loss changes with NRR, approximations to $\bar{L}(Df_w, \beta)$ from (31) are derived for both small and large values of β .

When β is small, a first-order MacLaurin series expansion to (31), after converting to a decibel loss, results in

$$-10 \log_{10} \bar{L}(Df_w, \beta) \approx 4.3 \beta \left\{ 1 - \frac{[1 - \cos(2\pi Df_w)]}{2\pi^2 (Df_w)^2} \right\} \quad (36)$$

$$\approx n_s (4.3 \gamma_r^2) \frac{(2\pi Df_w)^2}{12} \quad (37)$$

where the approximation from (36) to (37) assumes $Df_w \ll 1$. Thus, for low roughness and short pulses relative to the wave period, the per-reflection loss is constant and proportional to γ_r^2 and $(Df_w)^2$. For example, doubling pulse duration in this regime will result in a fourfold increase in the decibel MF loss.

When β is large or Df_w is small, the $\cos(v)$ term in (31) can be approximated by $1 - v^2/2$, yielding

$$\begin{aligned} \bar{L}(Df_w, \beta) & \approx \frac{1}{\pi Df_w} \int_0^{2\pi Df_w} \left(1 - \frac{v}{2\pi Df_w} \right) e^{-\beta v^2/2} dv \\ & = \frac{1}{\sqrt{2\beta\pi} Df_w} \left\{ 2\Phi(2\pi Df_w \sqrt{\beta}) - 1 \right. \\ & \quad \left. - \frac{1}{\sqrt{2\beta\pi} \pi Df_w} [1 - e^{-2\beta\pi^2 (Df_w)^2}] \right\} \end{aligned} \quad (38)$$

where $\Phi(z)$ is the standard normal cumulative distribution function. When $\beta \gg 1$, the term inside the braces in (38) tends to one and

$$\begin{aligned} -10 \log_{10} \bar{L}(Df_w, \beta) & \approx 4 + 10 \log_{10} \gamma_r + 5 \log_{10} n_s \\ & \quad + 10 \log_{10} (Df_w) \end{aligned} \quad (39)$$

which is essentially the result for $Df_w \gg 1$ from (35) with the addition of the term $10 \log_{10} (Df_w)$. The usefulness of this approximation can be seen from the $\sqrt{n_s} \gamma_r = 4$ case shown in Fig. 3, where (39) is the light blue line approximately from (0.1, 0) to (1, 10).

The approximation in (38) is quite good for small Df_w and large β . For example, the error is less than 0.1 dB when $Df_w \leq 0.8$ and $\beta \geq 5$ and also when $Df_w \leq 0.98$ and $\beta \geq 20$. Similarly, the small- β approximation in (36) is accurate when $\beta \ll 1$. Unfortunately, this leaves a region of moderate values of both β and Df_w for which the above approximations are not adequate. Fortunately, much of the structure observable in Fig. 3 is amenable to functional approximation. Clearly $\bar{L}(Df_w, \beta)$ tends to \bar{L}_∞ as $Df_w \rightarrow \infty$. Starting with this, and successively

approximating the residual errors, the function

$$\bar{L}(Df_w, \beta) \approx \bar{L}_\infty + \frac{(1 - \bar{L}_\infty) \text{sinc}^2(Df_w)}{1 + \beta[1 - \cos(2\pi Df_w)] g(\beta, Df_w)} \quad (40)$$

was found to provide an excellent fit to the integral in (31). The coefficients of the function

$$g(\beta, Df_w) = \frac{1}{6.2} - \frac{\beta}{501} + \cos(2\pi Df_w) \left[\frac{1}{71.8} + \frac{\beta}{735} \right] - \cos(4\pi Df_w) \left[\frac{1}{437} - \frac{\beta}{1490} \right] \quad (41)$$

found in the denominator of the latter term in (40) were obtained by a least-squared-error fit over a large region in β and Df_w . The approximation is shown in Fig. 3 as a dashed line and appears to overlay the numerical results. The fit error is less than one tenth of a decibel for (at least) the region defined by $\beta \leq 20$ and $Df_w \leq 4$. The largest errors generally occur in the regions $Df_w < 1$. The approximation should be used with care outside of this region, especially if $\beta > 20$.

3) *NB MF Loss for a Purely Sinusoidal Surface:* When the surface is purely sinusoidal, the amplitude in (10) is constant in both space and time (i.e., $A(t, \vec{x}) = A_w$). If there are many reflections, then $A_i = A_w$ for all of them in (12), but the CLT still dictates that $z(t)$ is Gaussian distributed when the ϕ_i are independent so the results of (31) and (32) will be valid.

However, if there is only one surface reflection and the phase is assumed to be uniformly random on $(0, 2\pi)$, the MF loss for reflection of a NB pulse from a purely sinusoidal surface can be obtained from (28) by removing the expectation over $y = A^2$. This results in

$$\begin{aligned} \bar{L} &= D^{-2} \int_0^D \int_0^D J_0(\sqrt{2}\gamma_r m(t-s)) dt ds \\ &= \frac{2}{D^2} \int_0^D (D-u) J_0(\sqrt{2}\gamma_r \sqrt{2-2\cos(\omega_w u)}) du \end{aligned} \quad (42)$$

where the amplitude A_w of the sinusoid enters through $\sigma_z = A_w/\sqrt{2}$ in γ_r . When Df_w is large, the asymptotic loss is approximately

$$\bar{L}_\infty \approx J_0^2(\sqrt{2}\gamma_r) \quad (43)$$

as shown in [9, App. B] where [24, eq. 6.684-1] can be used to simplify (42).

Recalling the similarity between the large- Df_w /small-effective-ensonified-area scenario and the small- Df_w /large-ensonified-area results for a Gaussian-distributed surface, it is not surprising that (43) is identical to the specular mode reflected from a sinusoidal surface in the latter scenario as described in [18, pg. 48].⁴

The asymptotic (large Df_w) MF loss for a single-surface reflection with a Gaussian-distributed height (via (32) with $n_s = 1$) is compared to the sinusoidal-surface result of (43) in Fig. 5.

⁴Note that the $\sqrt{2}$ in (43) accounts for γ_r being defined here using the RMS height, whereas the result in [18, pg. 48] uses the sinusoidal amplitude.

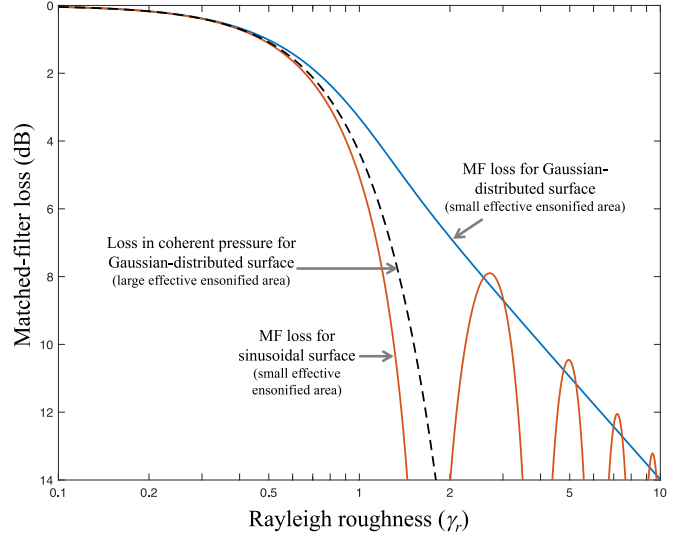


Fig. 5. Asymptotic MF loss (\bar{L}_∞) as a function of Rayleigh roughness (γ_r) for a single reflection from a Gaussian-distributed and sinusoidal surface height when the effective ensonified area is small. The average loss in coherent pressure for a Gaussian-distributed surface with a large ensonified area is also shown for comparison.

The higher loss incurred for the sinusoidal surface (e.g., for $\gamma_r \leq 2$) is expected because the Gaussian-distributed surface displacement is most likely to be observed near zero, while the sinusoidal surface is most likely to be observed near its extrema. For further comparison, the loss in coherent pressure from the classic result described in Section II-B is also shown.

C. Average Loss for Broadband LFM Pulses With a Time-Varying Surface

As previously mentioned, the primary application of this work requires the use of broadband signals (e.g., LFM or HFM waveforms) to induce a small effective ensonified area on the surface. The NB modeling presented in Section III-B can be extended to a broadband LFM pulse to result in a 2-D integral akin to (29) depending on Df_w , β , and the bandwidth-to-center-frequency ratio $\eta = W/f_c$

$$\begin{aligned} \bar{L}(Df_w, \beta, \eta) &= \int_{-\frac{1}{2}}^{\frac{1}{2}} \int_{-\frac{1}{2}}^{\frac{1}{2}} \exp \left\{ -\beta \left[1 - \cos(2\pi Df_w [u-v]) \right] \right. \\ &\quad \times (1 + \eta u)(1 + \eta v) \\ &\quad \left. + \frac{\eta^2}{2} (u-v)^2 \right\} du dv. \end{aligned} \quad (44)$$

Unfortunately, two of the approximations noted at the beginning of Section III-B, can cause the result in (44) to be inaccurate. When both Df_w and β are large, the reflected pulse can be distorted enough that the MF response $x(\tau)$ differs significantly from the waveform ACF in such a way that the peak response is at a different delay than that for the smooth surface. A secondary issue arises when Df_w is small and the temporal resolution capability of the LFM waveform is finer than the delay imparted

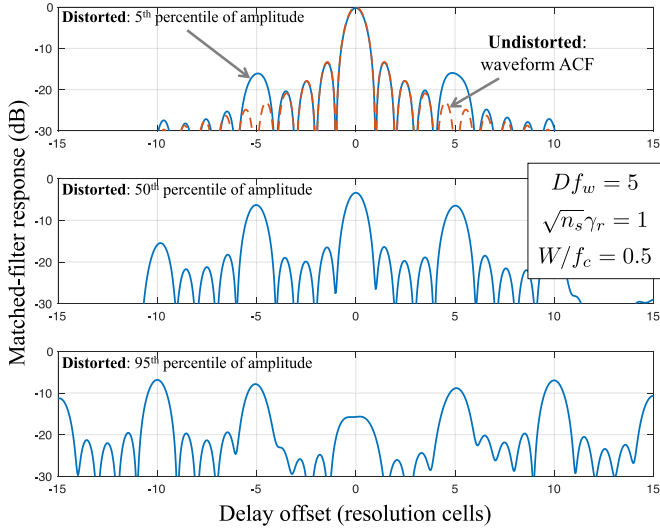


Fig. 6. Correlation function between LFM transmit pulse and a distorted reflected pulse for various effective surface wave amplitudes.

by the displaced surface. In both cases, the model was seen to overestimate the MF loss.

To illustrate how a distorted reflected signal produces a distorted MF response with a displaced peak, consider the net surface displacement from (16)

$$z(t) = \sqrt{2\sigma_z^2 n_s} A \cos(2\pi f_w t) \quad (45)$$

where the surface phase has been set to zero and the amplitude A is varied according to percentiles of the unit-power Rayleigh distribution. The MF response normalized by that for the smooth surface is shown in Fig. 6 for $Df_w = 5$, $\sqrt{n_s}\gamma_r = 1$, $W/f_c = 0.5$, and three values of the amplitude A . The top plot shows $A = 0.23$, which is a larger amplitude than only 5% of the Rayleigh-distributed occurrences, and exhibits a minor distortion in the form of a higher sidelobe in the response. The abscissa in Fig. 6 is the delay offset from the smooth-surface delay in terms of resolution cells, which is the product τW for an LFM pulse where τ is the actual delay offset. The high sidelobe occurs (approximately) at a delay offset of $\tau = Df_w/W$ (i.e., $\tau W = \pm Df_w = \pm 5$ in the example).

When $A = \sqrt{\pi}/2 = 0.83$, where half the Rayleigh-distributed amplitudes are above and half below, the highest sidelobe is still below the peak at zero delay offset and therefore does not violate the model assumptions. However, when $A = 1.73$, which is the 95th percentile of the unit-power Rayleigh distribution, the peak is no longer at zero delay offset and occurs instead at the sidelobe located ten resolution cells away. The implication is that the MF loss obtained under the assumption of the peak occurring at the same delay as for the smooth surface will be larger than that encountered by the Matched filtering process considering all possible delays. Varying the phase in (45) or W/f_c changes the response somewhat, but not the pertinent characteristics.

To determine the MF loss when all delays are evaluated, a simulation was performed as a function of NRR and $\eta = W/f_c$. The simulation implemented the MF described in (17) with

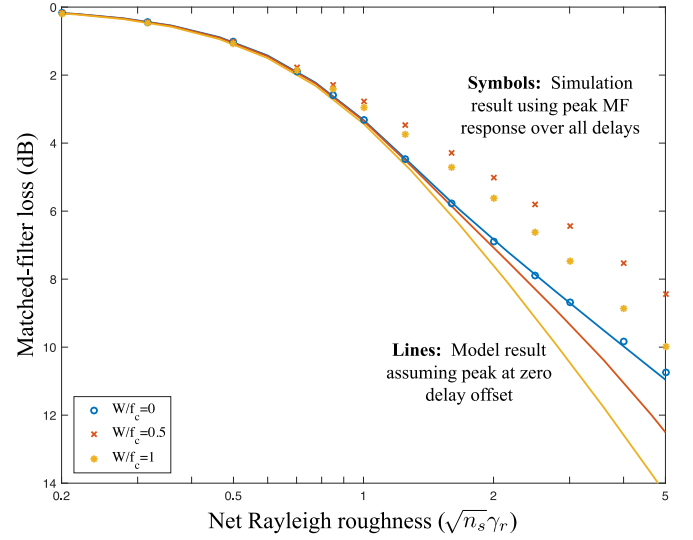


Fig. 7. MF loss from model assuming peak response occurs for zero delay offset compared with simulation result taking peak over all delays.

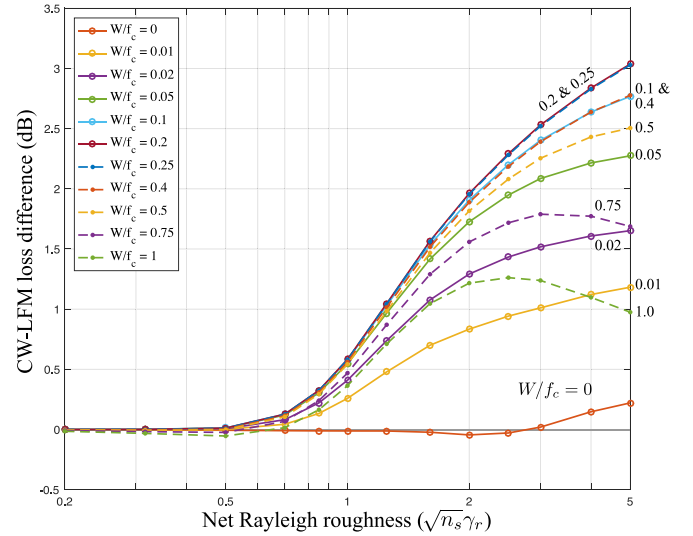


Fig. 8. Difference in MF loss between NB model and LFM-pulse simulation as a function of NRR and W/f_c .

$Df_w = 5$, $f_w = 0.25$ Hz, $f_c = 100$ Hz, 10^4 trials and an over-sampling factor of 15 to ensure the peak response was measured. The results for $W/f_c = 0, 0.5$, and 1 are shown in Fig. 7. For the CW pulse ($\eta = W/f_c = 0$), the model results are very accurate even up to an NRR of 5 where they differ by less than 0.25 dB. However, the LFM-pulse simulation results exhibit a significantly smaller loss than does the LFM-pulse model, in both cases exceeding a 3-dB difference at the highest NRR evaluated. The difference between the NB model and the LFM-pulse simulation results is shown in Fig. 8 for values of W/f_c ranging from zero to one. The figure illustrates that very little bandwidth in the LFM pulse is required for a significant difference between the NB model and the LFM-pulse simulation (e.g., the difference exceeds 1 dB at a 1% bandwidth to center frequency ratio when NRR exceeds 3). The difference peaks

for $\eta \approx 0.2$ with larger values being more accurately approximated by the NB model. The difference curve for $\eta = 0.5$ was approximated by the function

$$\Delta_L^{\text{dB}} \approx \max\left\{0, 1.11 - 0.527\sqrt{\beta} + 1.25\log(\beta)\right\} \quad (46)$$

which has a maximum absolute error of approximately 0.1 dB for $\text{NRR} \in [0.2, 5]$. The coefficients in (46) were formed by least-squared-error fitting for the values of NRR in the simulation exceeding 0.5 and truncated to three significant digits. This function can be used to approximate the difference between the NB-model asymptotic MF loss in (32) and that expected for an LFM pulse when $\eta \in [0.03, 0.7]$ with less than 0.65-dB absolute error for $\sqrt{\beta} \leq 5$. For the TREX13 data evaluated in Section IV where $\eta = 0.4$, the maximum error is less than one-eighth of a decibel.

IV. MODELING AND DATA ANALYSIS FOR TREX13

In this section, the models developed in Section III-B are applied to two scenarios from TREX13. In particular, predictions of MF loss are compared against the processed-data results reported in Hines *et al.* [9]. This section has four parts: Basic information on the TREX13 environment, sensing scenarios, and data processing are described in Section IV-A; the NB- and LFM-pulse model results from Sections III-B and III-C are applied to two TREX13 scenarios of interest in Section IV-B; modifications to the measurements reported in [9] required to account for geometric averaging are described in Section IV-C; and the model and data are finally compared in Section IV-D. Information regarding the broader TREX13 sea trials can be found in [16].

A. TREX13 Scenarios and Data

The sensing scenarios from [9] considered here include a short-range (~ 70 m) single surface reflection (S1) involving one-way propagation and an echo from a 2.8-km-distant passive acoustical target system (PATS echo)⁵ encountering a total of 12 surface reflections during two-way propagation. The source, receiver, and PATS were all fixed to the seabed, which had a nearly constant depth of 20 m, and the sound-speed profile was reasonably stable over the measurements. As such, the surface was expected to be the dominant source of fluctuations and MF loss. Details specific to the scenarios under consideration in this paper (e.g., the experiment, sonar equipment, sensing geometry, and data processing) can be found in [9]. The parameters required for the analysis presented here are found in Table I.

The transmit waveforms analyzed in [9] were 0.5- and 18-s duration LFM pulses with a 900-Hz bandwidth centered at 2250 Hz and a 10% Tukey shading (5% at both the beginning and end). The waveforms were transmitted at a repetition rate of 1 every 20 s over the course of six different 1-h acquisition periods (i.e., “runs”) for each pulse duration. The runs spanned a range of surface conditions providing Rayleigh roughness values of $\gamma_r \in (0.45, 1.2)$ for the S1 path and $\gamma_r \in (0.08, 0.21)$ for

TABLE I
PERTINENT INFORMATION FOR THE TREX13 ENVIRONMENT
AND SENSING SCENARIOS

Item	Value
Average speed of sound	$c_w = 1525$ m/s
Pulse duration	$D = 0.5$ and 18 s
Bandwidth	$W = 900$ Hz
Center frequency	$f_c = 2250$ Hz
Surface wave period	$f_w \in (0.2, 0.35)$ Hz
$D f_w$ for 0.5-s pulse	0.14
$D f_w$ for 18-s pulse	5
Grazing angle	S1: $\theta_g = 30^\circ$ /PATS: $\theta_g = 5^\circ$
Number of surface reflections	S1: $n_s = 1$ /PATS: $n_s = 12$

the PATS echo.⁶ As described in [9], the S1-path data were obtained from a single hydrophone in the receiving array while the PATS-echo data were obtained by beamforming the receiving array (48 triplet elements of the Five Octave Research Array [27] spaced at 0.2 m) with the main response axis pointed in the direction of the PATS. The remaining processing and analysis presented in [9] entailed Matched filtering followed by averaging the peak MF signal from each ping over 10-min windows (up to 30 pings) within each run. The 10-min-window averages (six per run) were used to produce a linear model fit to the peak MF response as a function of sea-surface RMS roughness (σ_z) as measured by a wave-rider buoy deployed and operated by the Applied Physics Laboratory of the University of Washington [28]. It is the linear model of the peak MF response as a function of RMS wave height from [9] that is taken for comparison with the models developed in this paper.

The 10-min averaging of the peak MF response performed in [9] was a compromise between a small window to reduce the impact of nonstationarity in the environmental conditions and a large enough window to reduce estimation error. To convey the uncertainty associated with the linear model of the average loss, a 90% confidence interval is constructed assuming the estimation errors in the linear-model parameters are Gaussian distributed and using the standard deviation of both the peak MF response and direct-blast measurements from [9] as a function of the RMS waveheight.⁷ The 90% confidence intervals, which are displayed as a gray shaded area around the TREX13 linear model in the figures, exhibit absolute errors in the 0.1–0.25 dB range (higher near the extremes of the RMS waveheight measurements and lower in the middle). These confidence intervals include both the inherent estimation error involved in estimating the linear-model parameters and any errors arising from nonstationarity of the environment within each 10-min measurement window.

1) *Effective-Ensonified-Area Analysis*: Using the formula from Section II-C, the effective ensonified down-range extent for the 900-Hz bandwidth pulse is $\mathcal{E}_{\parallel} \approx 1.7$ m for the PATS

⁶While the same runs are used to analyze both the S1 path and PATS echo, the different grazing angles lead to different values of γ_r .

⁷Note that the RMS waveheight measurements have been assumed to have no errors because they arise from 30-minute averages and the wave period is approximately $f_w \approx 0.3$ Hz which results in several hundred independent observations.

⁵In [9] the PATS echo was labeled “TE.”

TABLE II
EFFECTIVE ENSONIFIED EXTENT AND RANGE OF SCL MEASUREMENTS
(MINIMUM AND MAXIMUM OVER SIX RUNS) FOR
TREX13 SENSING SCENARIOS

Scenario	Direction	Effective ensonified extent (m)	SCL (m)	
			0.5-s Pulse	18-s Pulse
S1	down-range (\parallel)	1.9 (W)	1.5–6.6 (1)	1.5–6.2 (1)
S1	cross-range (\perp)	7.1 (F)	1.7–3.6 (6)	1.6–3.9 (6)
PATS	down-range (\parallel)	1.7 (W)	1.2–4.6 (1)	1.9–4.5 (0)
PATS	cross-range (\perp)	17.6 (F)	11.4–39.6* (3)	3.0–19.6* (4)

The effective ensonified extent is either limited by the waveform (W) or by the Fresnel zone width (F). The number in parentheses indicates how many of the six runs violate the small-effective-ensonified-area requirement. *Note: The PATS cross-range SCL is the distance between the peak of the SCF and the peak of the first negative sidelobe. All other SCLs are from [9].

echo and 1.9 m for the S1 path. The span of down-range (\parallel) SCL measurements from [9] are shown in Table II for the S1 (first row) and PATS (third row) scenarios. For most of the runs (10 of 12 for the 0.5-s pulse and 11 of 12 for the 18-s pulse) the down-range SCL is larger than the effective ensonified area.

Cross-range extent is limited by the Fresnel zone rather than by beamforming for the PATS echo or by the curvature of spherical spreading for the S1 path. The cross-range extent encompassing the first Fresnel zone⁸ is 7.1 m for the S1 path and 17.6 m for the PATS echo (for a single reflection). For the S1 path, the SCL measurements from [9] are less than 5 m for all of the runs (second row in Table II), so the small-effective-ensonified-area models of MF loss developed in Sections III-B and III-C are expected to predict less loss than that measured from the data. Following the arguments made in Section II-C regarding multiple consecutive reflections, the SCL for the PATS echo is defined by the distance in the cross-range dimension of the SCF to the first negative sidelobe (akin to a peak-to-trough distance). As seen in the last row of Table II, nearly half of the runs (3 of 6 for the 0.5-s pulse and 2 of 6 for the 18-s pulse) satisfied the small-effective-ensonified-area requirement.

Mitigating the concern of when the SCL measurements are less than the effective ensonified area is the observation that the longest lengths were measured when the sea surface was in one of the top two roughest conditions measured, indicating the model-data error will be lowest in the region where the most loss will be observable.

2) *Pulse Duration Re Wave Period*: From [9, Appendix B], the peak frequency of the sea-surface height power spectral density ranged from 0.2 to 0.35 Hz for the TREX13 runs under consideration. Using a nominal value of $f_w = 0.275$ Hz, the 0.5-s duration pulse has a very small value of $Df_w = 0.14$. From Fig. 3, the maximum loss expected to be observed in the TREX13 data for this pulse duration is less than 0.5 dB. This result corroborates the analysis presented in [9], where the 0.5-s-pulse peak MF level was shown to have a low correlation

⁸The first Fresnel zone width is calculated as two times the lateral distance at which the path difference is one half wavelength at f_c . This can be seen to be $2\delta_{\perp} \approx \sqrt{2\lambda_c z_s / \sin \theta_g}$ from (2) by letting $\Delta_r = \lambda_c/2$ with z and δ_{\parallel} set to zero.

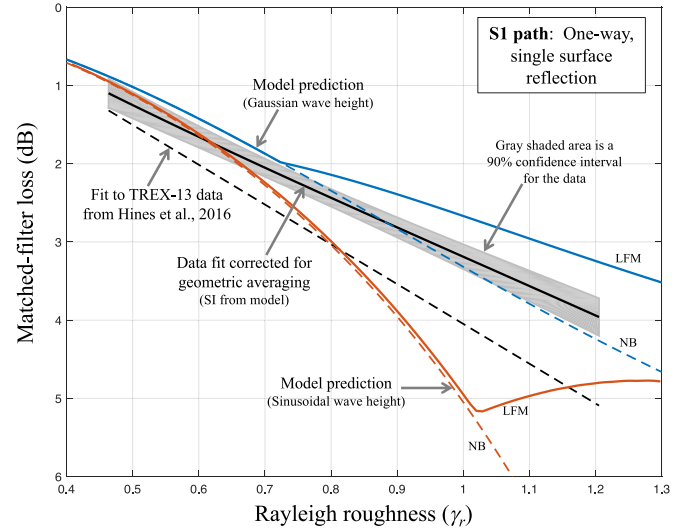


Fig. 9. MF loss model-data comparison for S1 path of TREX13 data.

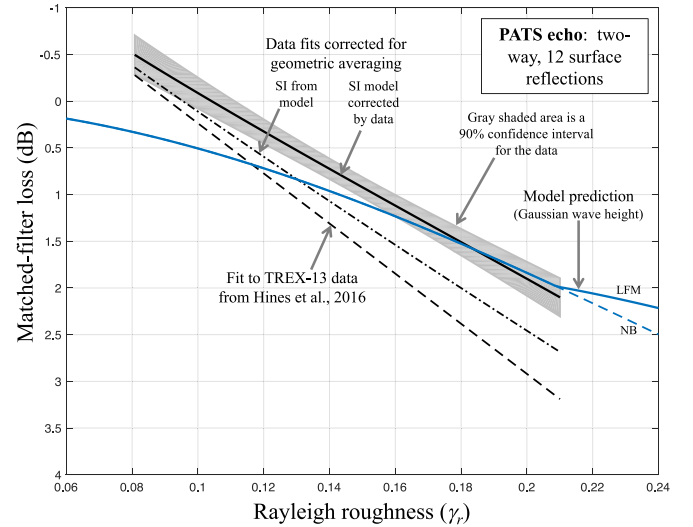


Fig. 10. MF loss model-data comparison for PATS echo of TREX13 data.

between the received level and σ_z . The remainder of this section therefore focuses on the 18-s duration pulse for which $Df_w \approx 5$.

B. Model Results for the TREX13 Scenarios

With $Df_w = 5$ for the 18-s duration pulse, the asymptotic results of (32) for the Gaussian-distributed net surface displacement and (43) for the sinusoidal surface are appropriate for consideration. These models are shown as the colored dashed lines in Figs. 9 and 10, respectively for the S1 path and PATS echo (note that the sinusoidal surface results are not evaluated for the PATS echo because of the 12 surface reflections). Because the transmit waveform was broadband and the models are for a NB pulse, the need for a bandwidth correction as described in Section III-C must be assessed.

By examining Fig. 8, it can be seen that little to no impact is expected for the PATS echo for which NRR will have maximum

value $\sqrt{12} \cdot 0.21 = 0.73$ and the NB model is within one quarter decibel of the LFM-pulse simulation for $\eta = 0.4$. However, the S1 path (for which NRR will have a maximum value of 1.2) shows approximately a 1-dB difference. This difference is incorporated into the NB models for the Gaussian-distributed surface displacement using (46) and shown in Figs. 9 and 10 as the solid blue line. A separate simulation similar to that described in Section III-C was performed for the sinusoidal surface model for the S1 path, but only for $\eta = 0.4$. The results are shown as the solid brown line in Fig. 9 and differ from the bandwidth effect seen for the Gaussian-distributed surface in that the NB-model results are accurate to a larger value of γ_r (approximately one) after which the decrease in loss is much more significant than for the Gaussian-distributed surface (i.e., the NB-model MF loss is very pessimistic).

C. Linear Models for Measured MF Loss From [9] and Geometric Averaging

The linear models fit to measurements of the peak MF response reported in [9, Fig. 17] for the two scenarios were adjusted in [9, App. B] to represent MF loss, resulting in

$$\begin{aligned}\hat{L}_{S1}^{\text{dB}} &= 47.17\sigma_z - 1.04 \\ &= 5.09\gamma_r - 1.04\end{aligned}\quad (47)$$

for the S1 path and

$$\begin{aligned}\hat{L}_{\text{PATS}}^{\text{dB}} &= 43.37\sigma_z - 2.45 \\ &= 26.84\gamma_r - 2.45\end{aligned}\quad (48)$$

for the PATS echo with units of decibels. The second line in (47) or (48) represents the function as a linear model in γ_r , obtained by modifying the slopes according to the definition of γ_r using the information found in Table I. These data results are the black dashed lines in Figs. 9 and 10. It is important to note that the data used to form the linear model contain some noise despite the 10-min averaging. Additionally, the y -intercept term for the PATS echo in (48) incorporates estimates of two-way transmission loss (120 dB) and the target strength of the PATS (6 dB). These complications explain the negative MF loss values exhibited in Fig. 10 and suggest a focus on the slopes of the functions for the PATS echo as opposed to the y -intercepts.

The averaging implemented in [9] over the 10-min windows was performed after the peak MF envelope had been converted to decibels (i.e., a geometric average). Such averaging is prudent to limit the effect of outliers when working with small sample sizes, but can introduce a bias in the measurement as described in [29]. An approximation to the bias for a Rician signal model [30] is derived in the Appendix. The bias ranges from zero (no bias) for a completely coherent signal (i.e., a deterministic or nonfluctuating signal) to -2.5 dB for a Gaussian-fluctuating signal. Because averaging in decibels produces an estimate that is expected to be lower than the true value, the MF loss functions in (47) and (48), which are formed by subtracting the decibel-averaged estimates, are biased high. The bias derived in the Appendix only depends on the scintillation index (SI) of the signal, which is the ratio of the variance of the instan-

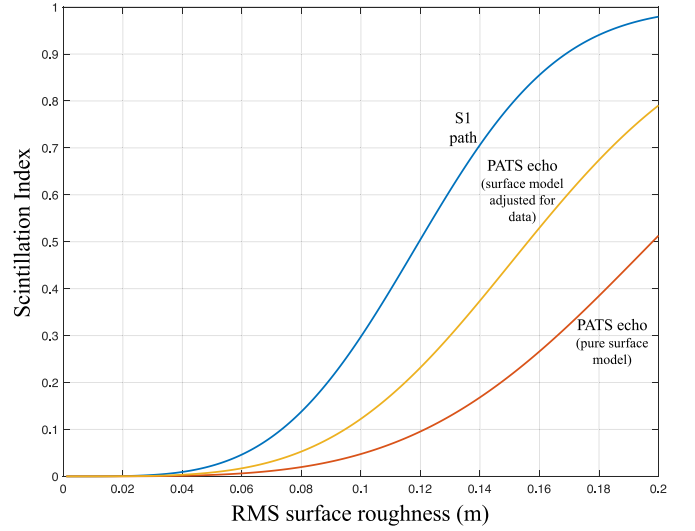


Fig. 11. Modeled SI as a function of RMS surface roughness for the S1 path and PATS echo of TREX13 data.

aneous intensity to its squared average. For the Rician signal model, SI depends on the ratio between the coherent (P_{coh}) and incoherent power (P_{inc}) in the MF response as described in (54) in the Appendix. The models derived in this paper represent the total power ($P_{\text{coh}} + P_{\text{inc}}$) while the coherent power under the small-effective-ensonified-area assumption can be shown to have the same form as that of the classical result ($P_{\text{coh}} \propto e^{-\beta}$). Using (32) for the large- Df_w , Gaussian-distributed net surface displacement case results in

$$\frac{P_{\text{coh}}}{P_{\text{inc}}} = \frac{1}{I_0(\beta) - 1}. \quad (49)$$

The Rician signal model assumption then yields

$$\text{SI} = 1 - [I_0(\beta)]^{-2} \quad (50)$$

which is shown in Fig. 11 as a function of the RMS surface roughness (σ_z) for the two TREX13 scenarios. As expected, the signal is purely coherent when $\sigma_z \rightarrow 0$ and fluctuations increase with σ_z . It is important to note the models in this paper do not account for any loss of coherence arising from reflection from the bottom. Estimates of SI for the PATS echo presented in [31, Fig. 1] indicate it should be approximately 0.3 for TREX13 Run 84 (which had the roughest surface with $\sigma_z = 0.128$ m) while (50) only predicts SI = 0.12. The higher SI observed in the data might arise from reflection off a rough bottom, but also might arise from failing to precisely meet the requirements for a small effective ensonified area or from the effects of multipath propagation. To account for the observed SI, the ratio $P_{\text{coh}}/P_{\text{inc}}$ was reduced by 4.37 dB so the model matched the Run-84 measurement from [31]. The resulting SI is the middle curve in Fig. 11. Estimates of SI for the S1 path are not available so only the model results are shown. However, there was no bottom interaction on the S1 path.

Using an SI calculation from (50) in the Rician-signal geometric-averaging bias from (55) in the Appendix allows comparison of the models developed in Sections III-B and III-C

with the data analysis reported in [9] as represented by (47) and (48). Rather than adjusting the MF loss model to account for the decibel-averaging bias, the linear models of the MF loss measurements were modified so as to present the expected MF loss, which is important for sonar performance modeling. These adjustments are the black solid line in Fig. 9 for the S1 path and the black dash-dot (SI as predicted by the model) and solid (SI model as corrected by data) lines in Fig. 10 for the PATS echo.

D. Model-Data Comparison

As can be seen from Figs. 9 and 10, the linear models of the TREX13 MF loss measurements from [9] (after correcting for the geometric-averaging bias) and the models developed in this paper are quite similar in terms of trends and levels. Based on the adjustments made in Sections IV-B and IV-C, the solid colored lines (the models) should be compared with the solid black lines (data after bias removal). The 90% confidence intervals (gray shaded region) for the linear model described in Section IV-A are only shown for the TREX13 results after bias removal. The confidence intervals are not intended to “accept” or “reject” the various models, particularly because the data are known to not precisely satisfy the requirement for an effective ensonified area less than the SCL of the surface. However, they are useful to represent the quality of the TREX13 measurements, which strengthens the relevance of a good model fit when the confidence interval is tight (as is the case here).

For the S1 path (see Fig. 9) the fit between the Gaussian-distributed net surface displacement model (blue solid line) and the data is always within 1 dB. While the NB-model result (blue dashed line) appears as a better fit, the incongruity may be explained as the effect of not precisely meeting the small-effective-ensonified-area requirements in the cross-range dimension. As noted in Table II, the SCL in the cross-range dimension for the S1 path was less than the effective ensonified extent for all six runs. This implies a larger MF loss because of the combination of reflections from multiple independent surface components, which would improve the fit between the LFM-pulse model (blue solid line) and the TREX13 linear model. Accounting for this in the NB model (blue dashed line) would also have the effect of increasing the MF loss, which would then degrade the quality of the fit with the TREX13 data.

While there appears to be more support for the Gaussian-distributed surface than the sinusoidal surface in Fig. 9, that the data lie between the two models may indicate the surface is not precisely either. These qualitative assessments are supported quantitatively by calculations of the average slope over the region of support of γ_r for the data. The slopes, calculated as changes in the MF loss relative to either γ_r or $\log_{10} \gamma_r$, are shown in Table III. The change relative to γ_r can be compared with the linear models from (47) and (48) while that relative to $\log_{10} \gamma_r$ can be compared with the approximations in Section III-B for the NB pulse (i.e., Fig. 4), where it is 10 when NRR is large. For the S1 path (second data column in Table III), the slope from the model (8.85) is similar to the asymptotic value

TABLE III
AVERAGE SLOPE OF MF LOSS [UNITS: dB] OVER THE REGION OF γ_r
SUPPORTED BY TREX13 DATA MEASUREMENTS ANALYZED IN [9]

Case	Note	S1 path change re:		PATS echo change re:	
		γ_r	$\log_{10} \gamma_r$	γ_r	$\log_{10} \gamma_r$
Model	Gaussian surf. / NB	4.56	8.85	12.85	4.48
Model	Gaussian surf. / LFM	3.21	5.92	12.85	4.48
Model	Sinusoidal surf. / NB	9.47	20.21	—	—
Model	Sinusoidal surf. / LFM	5.28	9.06	—	—
Data	linear model fit from [9]	5.09	9.78	26.84	8.99
Data	Geo. avg. / SI via model	3.86	7.35	23.58	7.84
Data	Geo. avg. / SI data adj.	—	—	20.09	6.68

(10) while the data (adjusted for geometric averaging) is smaller (7.35), possibly because of the effect of the LFM waveform for which the model calculation is 5.92.

The PATS-echo MF-loss comparison found in Fig. 10 is also seen to have less than 1 dB of error between the bias-corrected data and the model (solid lines). While the previously described limitations in the PATS-echo data limit the strength of this result, the slopes at the higher values of γ_r are very similar and the restriction of the data fitting to a linear model may cause the disparity at lower values of γ_r . As anticipated in Section IV-B, the NB model is adequate for the small values of NRR spanned by the data. This is seen in Fig. 10 where the LFM pulse and NB models do not differ significantly over the region of γ_r with data support and is evident in Table III, where both models exhibit the same average slope. Similar to the discussion for the S1 path, the LFM-pulse model may be more accurate than the NB model if it were possible to account for the effective ensonified extent in the cross-range dimension exceeding the SCL (from Table II, the small effective ensonified area assumption is violated in the cross-range dimension for the PATS scenario in four of the six runs.)

Removing the geometric-averaging bias from the linear models reported in [9] is clearly an important step in comparing the data with the models. As seen in Figs. 9 and 10, qualitatively the process improved the model-data fit both in terms of absolute level and slope. Unfortunately, the process requires assumptions about the statistical nature of the data (e.g., the Rician signal model and SI model used here). Quantitatively, the average slopes shown in Table III improved for both scenarios.

V. CONCLUSION

The focus of this paper has been on developing models for the loss incurred in Matched filtering when a broadband sonar pulse reflects off a rough surface that has motion on the same time scale as the pulse duration. The case considered was when the effective ensonified area on the surface is limited to a region smaller in extent than the SCL. Matched filtering the broadband pulse accomplishes this in the down-range dimension while several system and sensing conditions can enforce it in the cross-range dimension. Under the small-effective-ensonified-

area assumption, simple models were developed for the MF loss using a NB assumption in the analysis and a Gaussian-distributed net surface displacement. The Gaussian-distributed net surface displacement can arise naturally or from multiple consecutive reflections as a pulse travels down a waveguide when the surface is not Gaussian distributed. The models illustrate how MF loss from a time-varying rough surface increases with the Rayleigh roughness (γ_r), the number of consecutive surface reflections, and the product between pulse duration and the surface wave frequency (Df_w). With respect to Df_w , the loss saturates when Df_w exceeds one. Because of the focus on a small effective ensonified area, the models only depend on the surface RMS height (through γ_r) and do not require specific knowledge of the spatial correlation other than to satisfy the small-effective-ensonified-area requirement. While the models are simple to evaluate, approximations useful in sonar-equation analysis were derived and found in some cases to be similar to the classic large-effective-ensonified-area result (e.g., the $4.3\gamma_r^2$ dB per bounce loss when γ_r is small and Df_w large). These similarities support the assessment found in [9] of the equivalence between reflection of a long pulse (relative to the surface period) from a small effective ensonified area with the classic scenario of a large effective ensonified area.

The NB models were seen to be accurate for broadband waveforms when both the roughness and the bandwidth-to-center-frequency ratio were small. While the theory was applied to broadband LFM pulses, the model result could not be simplified beyond a 2-D integral and was found to over-estimate the MF loss because the MF response was distorted to a point where the peak shifted away from the delay associated with a smooth surface. Simulation results illustrated that the MF loss using the peak of the distorted response should always be less for a broadband LFM pulse than that predicted by the NB modeling, so the NB model can be used as an upper bound.

The models were then compared with data measurements from TREX13 reported by Hines *et al.* in [9] including both one-way/short-range/single-surface-reflection and two-way/longer-range/multiple-surface-reflection scenarios with both short and long pulse durations relative to surface wave period. The data and models were in agreement for both scenarios on a very low MF loss for the short pulse and very little dependence on γ_r over the range of observations. For the longer pulse duration, the models and data were always within one decibel, exhibiting a good fit in both level and slope. The minor disparity between the model and data is believed to arise from the effective ensonified extent in the cross-range dimension being larger than the SCL.

The models presented in this paper will be useful in predicting surface reflection loss for broadband waveforms when pulse duration is on par with or exceeds the surface wave period. When the small-effective-ensonified-area requirements are not met (most likely failing in the cross-range dimension), the models presented here can be taken as lower bounds on the MF loss. Finally, the NB model is most likely applicable as an approximation to HFM waveforms as well as the LFM; however, this has not been confirmed.

APPENDIX

BIAS INCURRED BY AVERAGING IN DECIBELS

Estimates of the MF loss obtained from the data analysis in [9] were formed as the sample mean after pressure measurements were converted to decibels. This implements a geometric averaging rather than a linear average and imparts a bias on the estimate depending on the statistical distribution of the MF response as described in [29]. Geometric averaging is both common and desirable because of its robustness against outliers observed in small samples from heavy-tailed distributions.

Reflection from a rough surface is often represented as producing both a coherent and an incoherent response. If the incoherent response can be approximated through a Gaussian-distributed random variable, this produces what is known as a Rician signal model [30]. For the Rician signal model, the instantaneous intensity T (i.e., the magnitude-squared MF response) is proportional to a noncentral chi-squared (NCCS) random variable

$$\frac{2T}{P_{\text{inc}}} = Y \sim \chi_{2,\delta}^2 \quad (51)$$

where $\delta = 2P_{\text{coh}}/P_{\text{inc}}$ is the noncentrality parameter, P_{inc} is the incoherent power of the signal and P_{coh} is the coherent power. The mean value of T is $\mu_T = P_{\text{coh}} + P_{\text{inc}}$. When the instantaneous intensity is converted to decibels before averaging, the measurement becomes

$$E[10 \log_{10} T] = 10 \log_{10} \mu_T + E \left[10 \log_{10} \left(\frac{Y}{2} \right) \right] - 10 \log_{10} \left[1 + \frac{P_{\text{coh}}}{P_{\text{inc}}} \right]. \quad (52)$$

The first term on the right side of (52) is the desired measurement while the latter two terms represent the bias.

When the incoherent component of the signal dominates the coherent component (i.e., $P_{\text{inc}} \gg P_{\text{coh}}$), the instantaneous intensity is approximately exponentially distributed and represents Gaussian signal fluctuations. For this situation, $Y/2$ is a unit-mean exponential random variable and the bias can be shown (using [24, 4.331-1] or from [29]) to be

$$B_{\text{dB}} = \frac{10 \psi(1)}{\log(10)} \approx -2.5 \quad (53)$$

where $-\psi(1) \approx 0.5772$ is Euler's constant and $\psi(\cdot)$ is the digamma function [26, Ch. 44]. Within the context of the NCCS-distributed instantaneous intensity, this represents the largest bias expected to be encountered. Thus, averaging in decibels can result in up to a 2.5-dB bias lower than the actual value for the NCCS signal model mean.

No simple closed-form result appears to be available for the more general NCCS model. An approximate solution can be obtained by noting the gamma distribution can be used to represent the NCCS distribution [32, Sec. 29.8]. If $T \sim \text{Gamma}(\alpha, \beta)$, matching moments with the NCCS characterization results in

$\alpha = 1/\text{SI}$ where

$$\text{SI} = \frac{1 + 2P_{\text{coh}}/P_{\text{inc}}}{(1 + P_{\text{coh}}/P_{\text{inc}})^2}. \quad (54)$$

As will be seen, the Gamma scale parameter, $\beta = \mu_T/\alpha$, is not used in determining the estimator bias. Using [24, 4.352-1] and assuming T is gamma distributed, the bias term can be shown to be

$$\begin{aligned} B_{\text{dB}} &= E \left[10 \log_{10} \left(\frac{T}{\mu_T} \right) \right] \\ &= \frac{10}{\log(10)} [\psi(\text{SI}^{-1}) + \log(\text{SI})]. \end{aligned} \quad (55)$$

Thus, when the signal is completely coherent, $\text{SI} = 0$ and $B_{\text{dB}} = 0$. When the incoherent component dominates, $\text{SI} = 1$ and B_{dB} simplifies to the -2.5 dB result shown in (53). In between ($0 \leq \text{SI} \leq 1$), B_{dB} is nearly linear in SI (the maximum error to a linear fit is less than 0.1 dB).

Using [24, 4.358-5], it can also be shown that the variance of the decibel calculation of the instantaneous intensity through the gamma approximation to the Rician signal is

$$\text{Var}\{T_{\text{dB}}\} = \left(\frac{10}{\log 10} \right)^2 \psi'(\text{SI}^{-1}) \quad (56)$$

where $\psi'(\cdot)$ is the trigamma function [26, Ch. 44]. For a fully saturated signal (i.e., $\text{SI} = 1$), this yields the familiar standard deviation of 5.6 dB that was derived in [29].

ACKNOWLEDGMENT

The authors would like to thank P. Hines, J. Scrutton, and S. Murphy of Defence Research and Development Canada-Atlantic who designed and conducted the portion of the TREX13 experiment from which the data in Section IV were obtained; D. Tang, T. Hefner, and K. Williams of the Applied Physics Laboratory of the University of Washington (APL-UW) who managed and led the TREX13 trial, and J. Preston of Pennsylvania State University's Applied Research Lab who managed quality control and data collection for the experiment. The authors would also like to thank the officers and crew aboard CFAV QUEST and RV SHARP, and the APL-UW dive team for their support throughout the trial. Funding for the TREX13 experiment was provided by ONR Code 32 and ONR Global-London. Finally, the authors would like to thank P. Dahl and D. Dall'Osto from APL-UW for providing data obtained from the wave buoy and their assistance in processing and interpreting it.

REFERENCES

- [1] H. W. Marsh, M. Schulkin, and S. G. Kneale, "Scattering of underwater sound by the sea surface," *J. Acoust. Soc. Amer.*, vol. 33, no. 3, pp. 334–340, Mar. 1961.
- [2] M. A. Ainslie, *Principles of Sonar Performance Modeling*. New York, NY, USA: Springer-Verlag, 2010.
- [3] C. Eckart, "The scattering of sound from the sea surface," *J. Acoust. Soc. Amer.*, vol. 25, no. 3, pp. 566–570, 1953.
- [4] H. Medwin and C. S. Clay, *Fundamentals of Acoustical Oceanography*. Boston, MA, USA: Academic, 1998.
- [5] X. Lurton, *An Introduction to Underwater Acoustics*. Berlin, Germany: Springer-Praxis, 2002.
- [6] J. A. Knauss, *Introduction to Physical Oceanography*, 2nd ed. Long Grove, IL, USA: Waveland Press, Inc., 1997.
- [7] H. A. DeFerrari, "Observations of low-frequency temporal and spatial coherence in shallow water," *J. Acoust. Soc. Amer.*, vol. 125, pp. EL45–EL49, 2009.
- [8] P. C. Hines, "Experimental comparison of continuous active and pulsed active sonars in littoral waters," in *Proc. 1st Int. Conf. Exhib. Underwater Acoust.*, Corfu, Greece, 2013, pp. 51–58.
- [9] P. C. Hines, S. M. Murphy, D. A. Abraham, and G. B. Deane, "The dependence of signal coherence on sea surface roughness for high and low duty cycle sonars in a shallow water channel," *IEEE J. Ocean. Eng.*, vol. 42, no. 2, pp. 298–318, Apr. 2017.
- [10] R. S. Keiffer, J. C. Novarini, and R. W. Scharstein, "A time-variant impulse response method for acoustic scattering from moving two-dimensional surfaces," *J. Acoust. Soc. Amer.*, vol. 118, no. 3, pp. 1283–1299, Sep. 2005.
- [11] M. Siderius and M. B. Porter, "Modeling broadband ocean acoustic transmissions with time-varying sea surfaces," *J. Acoust. Soc. Amer.*, vol. 124, no. 1, pp. 137–150, Jul. 2008.
- [12] B. E. Parkins, "Coherence of acoustic signals reradiated from the time-varying surface of the ocean," *J. Acoust. Soc. Amer.*, vol. 45, no. 1, pp. 119–123, 1969.
- [13] D. R. Dowling and D. R. Jackson, "Coherence of acoustic scattering from a dynamic rough surface," *J. Acoust. Soc. Amer.*, vol. 93, no. 6, pp. 3149–3157, Jun. 1993.
- [14] R. W. Scharstein and R. S. Keiffer, "Coherence function for the stochastic scattering by a time-varying, slightly rough, acoustically soft surface," *J. Acoust. Soc. Amer.*, vol. 126, no. 2, pp. 607–611, 2009.
- [15] D. A. Abraham, S. M. Murphy, P. C. Hines, and A. P. Lyons, "Matched-filter loss from time-varying rough-surface reflection with a small ensonified area," in *Proc. MTS/IEEE Oceans Conf.*, Monterey, CA, USA, 2016, doi: 10.1109/OCEANS-Genova.2015.7271240.
- [16] B. T. Hefner and D. Tang, "Overview of the reverberation component of TREX13," in *Proc. 2nd Underwater Acoust. Conf.*, Rhodes, Greece, Jun. 2014, pp. 707–713.
- [17] I. Tolstoy and C. S. Clay, *Ocean Acoustics: Theory and Experiment in Underwater Sound*. New York, NY, USA: AIP, Inc., 1987.
- [18] P. Beckmann and A. Spizzichino, *The Scattering of Electromagnetic Waves from Rough Surfaces*. New York, NY, USA: Pergamon, 1963.
- [19] R. H. Stewart, *Introduction To Physical Oceanography*. Orange Grove Texts Plus, 2008.
- [20] N. Mukhopadhyay, *Probability and Statistical Inference*. New York, NY, USA: Marcel Dekker, 2000.
- [21] R. O. Nielsen, *Sonar Signal Processing*. Norwood, MA, USA: Artech House, 1991.
- [22] A. W. Rihaczek, "Principles of high resolution radar," New York, McGraw-Hill Book Company, 1969.
- [23] E. J. Kelly and R. P. Wishner, "Matched-filter theory for high-velocity accelerating targets," *IEEE Trans. Military Electron.*, vol. Mil-9, no. 1, pp. 56–69, Jan. 1965.
- [24] I. S. Gradshteyn and I. M. Ryzhik, *Table of Integrals, Series, and Products*, 8th ed., D. Zwillinger, Ed. Waltham, MA, USA: Elsevier Academic Press, 2015.
- [25] A. D. Jones, A. J. Duncan, A. L. Maggi, D. W. Bartel, and A. Zinoviev, "A detailed comparison between a small-slope model of acoustical scattering from a rough sea surface and stochastic modeling of the coherent surface loss," *IEEE J. Ocean. Eng.*, vol. 41, no. 3, pp. 689–708, Jul. 2016.
- [26] K. Oldham, J. Myland, and J. Spanier, *An Atlas of Functions*. 2nd ed., New York, NY, USA: Springer-Verlag, 2009.
- [27] K. M. Becker and J. R. Preston, "The ONR five octave research array (FORA) at Penn State," in *Proc. IEEE/MTS OCEANS Conf.*, 2003, vol. 5, pp. 2607–2610.
- [28] P. H. Dahl and D. R. Dall'Osto, "Observations of sea surface waves during the 2013 Target and Reverberation Experiment (TREX13) and relation to mid-frequency sonar," *IEEE J. Ocean. Eng.*, vol. 42, no. 2, pp. 250–259, Apr. 2017.
- [29] I. Dyer, "Statistics of sound propagation in the ocean," *J. Acoust. Soc. Amer.*, vol. 48, no. 1B, pp. 337–345, 1970.
- [30] S. O. Rice, "Mathematical analysis of random noise," *Bell Syst. Tech. J.*, vol. 23, no. 3, pp. 282–332, Jul. 1944.
- [31] D. A. Abraham and P. C. Hines, "Effect of pulse duration on echo matched-filter statistics in a shallow-water channel," *IEEE J. Ocean. Eng.*, vol. 42, no. 2, pp. 319–334, Apr. 2017.
- [32] N. L. Johnson, S. Kotz, and N. Balakrishnan, *Continuous Univariate Distributions*. vol. 2, 2nd ed., New York, NY, USA: Wiley, 1995.

Douglas A. Abraham (S'92–M'93–SM'04) received the B.S., M.S., and Ph.D. degrees in electrical engineering and the M.S. degree in statistics from the University of Connecticut, Storrs, CT, USA.

He is currently the President of CausaSci LLC, Ellicott City, MD, USA, and has previously held positions at the Naval Undersea Warfare Center (New London, CT, USA), the NATO SACLANT Undersea Research Center (La Spezia, Italy), the University of Connecticut, and the Applied Research Laboratory, Pennsylvania State University including an intergovernmental personnel assignment to the Office of Naval Research. His work is primarily in the area of statistical signal processing applied to underwater acoustics applications. His current research interests are in characterizing and accounting for clutter and environmental effects in active sonar signal-processing algorithms for detection, classification, and localization.

Stefan M. Murphy received the B.Sc. (honors) degree in physics from Acadia University, Wolfville, NS, Canada, in 2006 and the M.A.Sc. degree in mechanical engineering from Dalhousie University, Halifax, NS, Canada, in 2008.

He is currently a Scientist in the Sonar and Anti-Submarine Warfare Group, Defence Research and Development Canada, Dartmouth, NS, Canada, working in the field of active sonar signal processing and focusing on experimentation at sea.



Paul C. Hines was born and raised in Glace Bay, NS, Canada. He received the B.Sc. (honors) in engineering-physics from Dalhousie University, Halifax, NS, Canada, in 1981, and the Ph.D. degree in physics from University of Bath, Bath, U.K., in 1988.

In 1981, he joined Defence Research and Development Canada (DRDC), Dartmouth, NS, Canada. From 1985 to 1988, he was with the University of Bath. From his return to DRDC in 1988 until his departure in March 2014, he led several groups and

managed a variety of acoustic research projects for both DRDC and the U.S. Office of Naval Research. He is a Seasoned Experimentalist and has been the Chief Scientist for several collaborative international research trials. He is currently the President of Hines Ocean S&T, Inc., in addition to conducting research at Dalhousie University in the Department of Electrical and Computer Engineering and Department of Oceanography. His research interests include Anti-Submarine Warfare, mine and torpedo countermeasures, rapid environmental assessment, acoustic scattering, sound speed dispersion, vector sensor processing, sonar classification and tracking, continuous active sonar, and the application of aural perception in humans, to target classification in sonar.

Dr. Hines is a Fellow of the Acoustical Society of America, and a Distinguished Lecturer of the IEEE Ocean Engineering Society. He received the Chesterman Medal from the University for Outstanding Research in Physics for his research on acoustic scattering from ocean boundaries.

Anthony P. Lyons (M'96) received the B.S. degree in physics from Henderson State University, Arkadelphia, AR, USA, in 1988 and the Ph.D. degree in oceanography from Texas A&M University, College Station, TX, USA, in 1995.

After receiving the Ph.D. degree, he worked in the Fine-Scale Acoustics and Oceanography Group, SACLANT Undersea Research Center, La Spezia, Italy, from 1995 to 2000, where he was involved in a variety of projects in the area of environmental acoustics. Prior to taking his position at the University of New Hampshire, he was a Senior Scientist in the Applied Research Laboratory, Penn State, and a Professor of acoustics in Penn States Graduate Program in Acoustics. He also worked for short periods in 2008 and 2014 for the U.S. Office of Naval Research Global. His research projects have included studies of shallow-water acoustic propagation, acoustic interaction with the seafloor, characterization of seafloor sediments, and high-resolution oceanographic measurements.

Dr. Lyons is a Fellow of the Acoustical Society of America (2007) and a member of the IEEE Oceanic Engineering Society. He is also currently an Associate Editor for the Journal of the Acoustical Society of America. He received the recommendation of the Acoustical Society of America, the Institute of Acoustics' (U.K.) A.B. Wood Medal in 2003.